공학석사 학위논문

Application of Magnetic Resonance Imaging for Aerothermal Analysis of Impinging Jet Mixing Flow

자기공명영상법의 적용을 통한 충돌 제트 혼합 유동의 열/유동 분석

2020년 8월

서울대학교 대학원

기계항공공학부

류 형 우

Application of Magnetic Resonance Imaging for Aerothermal Analysis of Impinging Jet Mixing Flow

자기공명영상법의 적용을 통한 충돌 제트 혼합 유동의 열/유동 분석

지도교수 황 원 태

이 논문을 공학석사 학위논문으로 제출함

2020년 4월

서울대학교 대학원

기계항공공학부

류 형 우

류형우의 공학석사 학위논문을 인준함

2020년 6월

위 원 장 최 해 천 (인)

부위원장 황 원 태 (인)

위 원 김 호 영 (인)

Abstract

Aerothermal analysis of complex flow systems requires thorough analysis. However, traditional measurement methods have limitations and pose hardships when measuring three-dimensional aerothermal properties. Such limitations can be overcome using non-intrusive magnetic resonance based measurement techniques. In this study, magnetic resonance velocimetry (MRV) / thermometry (MRT) is utilized to measure three-dimensional mean velocity and temperature fields of a complex flow system simulating the dilution zone of a gas turbine combustor.

For basic verification of the techniques, a fully developed turbulent pipe flow is analyzed and the results are compared with numerical results and other measurement data. MRV velocity profile in the fully developed region is compared with direct numerical simulation (DNS) data, and MRT results are compared with thermocouple data for verification.

For the combustor dilution zone analysis, radial jets are injected into a pipe flow, and upstream penetration and jet-like flow structure downstream are observed due to jet collision. The jet-like flow structure is compared with a round free jet through self-similarity analysis. Similar trend in flow development is observed in terms of normalized velocity profiles. Also, the correlation between thermal mixing and momentum flux ratio is further analyzed by comparing results of three different momentum flux ratios.

Keyword : Magnetic resonance velocimetry, Magnetic resonance thermometry, Aerothermal analysis, Gas turbine combustor, Phase contrast, Proton resonance frequency shift
Student Number : 2018-28838

Table of Contents

List of Figures

List of Tables

Nomenclature

B_0	External magnetic field strength ($kg \cdot s^{-2} \cdot A^{-1}$)
B_l	Shifted magnetic field strength ($kg \cdot s^{-2} \cdot A^{-1}$)
CFD	Computational fluid dynamics
DNS	Direct numerical simulation
D_h	Hydraulic diameter
FA	Flip angle (^{o})
FC	Flow compensation
FT	Fourier transform
G	Gradient field
GRE	Gradient echo
IR	Infrared
J	Momentum flux ratio
LIF	Laser-induced fluorescence
M	Mole (mol)
MR	Magnetic resonance
MRT	Magnetic resonance thermometry
MRV	Magnetic resonance velocimetry
NMR	Nuclear magnetic resonance
NSA	Number of signal averaging
PIV	Particle image velocimetry
PRF	Proton resonance frequency
ROI	Region of interest
Re	Reynolds number
RF	Radio frequency

PRF	Proton resonance frequency
T	Tesla ($kg \cdot s^{-2} \cdot A^{-1}$)
TE	Echo time (ms)
TR	Repetition time (ms)
R	Pipe radius (mm)
r	Radial distance (mm)
u	Streamwise velocity (cm/s)
u_{max}	Maximum streamwise velocity (cm/s)
α	MRT linearity constant
β	Local voxel area
γ	Gyromagnetic ratio ($rad \cdot s^{-1} \cdot T^{-1}$)
ϕ	Signal phase data

Chapter 1. Introduction

1.1. Research Background

Analysis of complex flow systems, such as gas turbine engine or heat exchanger, has been one of the most challenging tasks in numerous fields of engineering due to difficulties in measurements posed by complex flow geometry and extreme flow conditions. Traditional aerothermal measurement techniques such as pitot tube and thermocouple are intrusive and other techniques such as particle image velocimetry (PIV), infrared (IR) or laser-induced fluorescence (LIF) thermography are often limited to 2D measurements. In such complex flows, interference between flow and measurement probes can cause alteration of flow structure downstream, which is directly related to measurement errors. Although PIV and LIF are known to be non-intrusive measurement techniques, these methods still hold limitations as they require additional optical windows and relatively simple flow passages to avoid surface reflections and distortion in data. Also, computational fluid dynamics (CFD) is frequently used for the analysis of complex flows to overcome experimental limitations. However, CFD requires high computation power and considerable time to solve for an approximate solution. Furthermore, the result must be validated for complex flows with other experimental data. To resolve such problems, there has been a constant need for non-intrusive 3D

measurement techniques. This can be achieved by utilizing magnetic resonance (MR) measurement techniques.

In the medical industry, magnetic resonance imaging (MRI) has been used for imaging of tissues in the body for a long time. MRI is capable of capturing physical properties non-intrusively by measuring the resonance signals of protons placed inside the magnetic field. There have been numerous attempts in applying MR techniques to the fields of engineering for aerothermal analyses. For velocity field analysis, Elkins et al. [1] utilized an MR based measurement technique known as magnetic resonance velocimetry (MRV) to capture flow motion and obtained 3D mean velocity field of a complex flow. Benson et al. [2] also applied MRV on the analysis of gas turbine blade trailing edge film cooling flow.

Magnetic resonance thermometry (MRT), an MR based temperature measurement technique, has also been derived from the medical field. Initially, studies have been conducted to measure the temperature of the body using MR for the safety of patients when the temperature of a local area in the body rises during hyperthermia therapy for cancer treatment [3, 4]. Wassermann et al. [5] further developed the technique and have shown that MRT is applicable to the engineering field by measuring the 3D mean temperature field of a flow in a circular tube. Spirnak et al. [6] conducted MRT measurement of jet in a crossflow, where flows of different temperatures are mixed, and compared the result with previous experimental data for validating MRT. Also, Benson et al. [7] applied

MRT on the analysis of gas turbine blade. Since the measurement results are dependent on both proton movement and temperature, previous studies have focused on finding ways to minimize the experimental errors by shortening the measurement time and as a result, numerous ways of data processing and measurement methods have been suggested.

1.2. Research Objective

In the present study, aerothermal analyses of a fully developed turbulent pipe flow are first conducted with MRV and MRT using 3T and 7T MRI machines for fundamental verification of the techniques. Velocity profile of the flow is measured using MRV and verified by comparing the result with direct numerical simulation (DNS) data. Next, MRT measurement is conducted and the results are compared with temperature measured with thermocouples for verification. Data correction method using reference oil phantom to remove measurement errors due to system bias is also presented.

After technique verification, impinging jet mixing flow consisting of radially injected jets in a crossflow is examined to simulate and understand the physics of complex flow in a gas turbine combustor dilution zone. In a dilution zone, jets are injected radially to lower the mean temperature and eliminate extreme temperature gradient to avoid damage due to thermal fatigue. It is critical to find an optimal flow condition for efficient flow mixing without too much aerothermal

loss. The effects of momentum flux ratio between the radial jets and main pipe flow on mixing characteristics are examined through self-similarity analysis and comparison of temperature non-uniformity.

Chapter 2. Experimental Method

2.1. MR Measurement Principles

MR measurement techniques derive from resonance signals emitted from protons within a magnetic field. To generate resonance signals, random magnetic moment of nuclei is first aligned along the external magnetic field (B_0) of the MRI machine. This process is called longitudinal magnetization. Radio-frequency (RF) excitation pulse is then applied to make the nuclei resonate and initiate precession of the magnetic moment. The specific frequency, known as Larmor frequency (ω) [8], is determined by the following Equation 2.1, where γ is the gyromagnetic ratio of nuclei and B_0 is the strength of the external magnetic field exerted by the MRI machine.

$$\omega = \gamma B_0 \qquad \textit{Equation } 2.1$$

Required RF pulse frequency differs depending on type of nuclei and magnetic field strength. Once the protons are excited, precession of the net magnetic moment with angular frequency of ω takes place at certain flip angle (FA) with respect to the direction of the magnetic field. MRV and MRT techniques utilize phase change of the signals due to movements or temperature change.

It is possible to measure 3D field using magnetic field gradients

as shown in Figure 2.1. Based on the idea of Larmor frequency, applying linearly varying magnetic field along the region of interest (ROI) allows localization of specific location for measurements. For 3D measurements, magnetic field gradients can be applied in three different directions. First, slice selection gradient is applied in main flow direction. Slice selection usually determines the thickness of a measurement plane. Each of the frequency encoding and phase encoding gradients correspond to x−axis and y−axis in Fourier domain. The measured signal frequency datasets are then converted into an image data through inverse Fourier transformation. Multiple sets of planar measurement data can be combined to obtain 3D field data.

For MR measurement, time interval between each RF pulse excitation is known as repetition time (TR). TR is the amount of time required for each measurement period consisting of RF pulse excitation, data acquisition, and longitudinal magnetization recovery. Echo time (TE) is the time interval between RF pulse excitation and data acquisition.

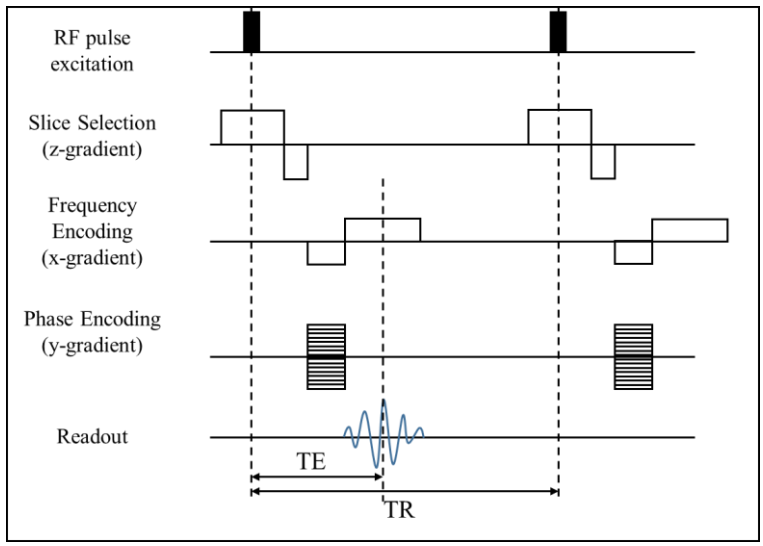

Figure 2.1. Gradient echo sequence diagram

2.2. Magnetic Resonance Velocimetry (MRV)

MRV is a non-intrusive MR measurement technique, which measures signal phase change due to motion within the ROI. Net phase change can be expressed by Equation 2.2 with Taylor series expansion. For simplicity, higher order terms including acceleration term are neglected.

$$\phi(\vec{r},TE) = \phi_0 + \gamma \int_0^{TE} \vec{r_0} \cdot \vec{G}(t)\, dt + \gamma \int_0^{TE} \vec{v} \cdot \vec{G}(t)\, tdt \qquad Equation\ 2.2$$

ϕ is the signal phase, γ is gyromagnetic ratio, $\vec{r}_0$ is the position, $\vec{v}$ is velocity, and $\vec{G}$ is the magnetic field gradients. The third term on the right hand side represents the phase shift due to motion within the magnetic field. Higher order momentum terms are neglected for

simplicity in the current study.

In order to obtain 3D velocity components of a flow, a set of measurements is required. First, MR scan is conducted while the protons are moving. Then, another scan is accompanied when the fluid is stationary. The latter signal phase data is subtracted from the initial phase data to remove any additive velocity errors due to remaining eddy current or magnetic field-related imperfections during the measurement [1]. A bipolar gradient, a pair of magnetic gradients with same magnitude but opposite polarity, is applied to gain net phase shift of moving nuclei but zero phase change for stationary nuclei. By setting velocity encoding (VENC) value slightly higher than the maximum velocity, phase change due to motion within $\pm\pi$ range is converted into velocity proportionally.

2.3. Magnetic Resonance Thermometry (MRT)

Using MRT, it is possible to calculate 3D mean temperature field from the signal phase shift. Equation 2.3 is derived from the second term on the right hand side of Equation 2.2, which represents the proton resonance frequency (PRF) shift due to temperature change.

$$\begin{aligned}\phi(\vec{r},TE) &= \gamma\int_0^{TE}\{B_l+\vec{G}(t)\cdot\vec{r}\}\,dt \\ &= \gamma\int_0^{TE}\{(1-\sigma(\vec{r}))B_0+\vec{G}(t)\cdot\vec{r}\}dt \end{aligned} \qquad \textit{Equation } 2.3$$

As the temperature changes, proton experiences magnetic field strength (B_l) slightly different from the external magnetic field strength (B_0) by the portion of $\sigma(\vec{r})$ due to nuclear shielding effect [9]. Signal phase shift under different temperature conditions can be expressed as Equation 2.4.

$$\begin{aligned}\Delta\phi &= \phi_1(\vec{r},TE) - \phi_2(\vec{r},TE) \\ &= \gamma \int_0^{TE} (\sigma_1(\vec{r}) - \sigma_2(\vec{r}))B_0 dt \\ &= \gamma\Delta\sigma(\vec{r})B_0TE \\ &= \gamma\alpha\Delta T(\vec{r})B_0TE \end{aligned} \qquad Equation\ 2.4$$

From this approach, a new variable, PRF thermal constant, α, which represents the linearity between signal phase shift and temperature change, is introduced. For simplification, Equation 2.4 can be rearranged to Equation 2.5.

$$\Delta T = \frac{\phi(TE) - \phi_{baseline}(TE)}{\gamma\alpha B_0 TE} \qquad Equation\ 2.5$$

where $\phi_{baseline}(TE)$ is the measured signal phase at reference temperature and $\phi(TE)$ is the measured signal phase at target temperature. TE must be chosen according to the dynamic range of temperature to avoid any aliasing since other parameters cannot be changed.

As one can tell from the equation above, MRT does not measure

the absolute temperature, but rather measures the change in temperature from the PRF shift so temperature must be known at least at one location to be able to calculate absolute temperature of the ROI.

In the previous studies [10-13], precise nuclear magnetic resonance (NMR) experiments were conducted and $\alpha = -0.01$ ppm/°C was determined for pure water.

The resultant phase data, however, is dependent on both fluid motion and temperature as mentioned earlier. In order to measure temperature correctly using MRT technique under "flow on" condition, velocity effects must be removed to solely measure the effect of temperature. This problem can be resolved by using flow compensation (FC) technique. FC is a technique that can cancel out velocity effects by adding additional magnetic gradient lobes during data acquisition [14] as shown in Figure 2.2.

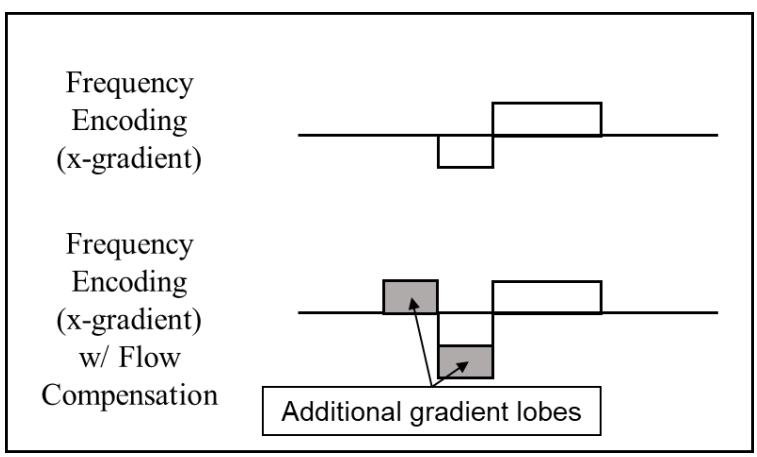

Figure 2.2. Flow compensation diagram

Chapter 3. Experimental Setup

3.1. Fully Developed Turbulent Pipe Flow

A schematic of the flow system used in this study is shown in Figure 3.1 and one of the MRI machines and experimental setup used for the study is shown in Figure 3.2. Pump, valves, and bypass loop are used to control the flow. Seametrics SPX-100 impeller flowmeter and K-type thermocouple are installed to measure the volumetric flow rate and temperature. A 25A size hose with length of 30 m and 3.5 mm thickness is used to transport water from the reservoir to the test section. In order to minimize temperature fluctuations during the experiment, 200 L water reservoir is used and temperature is controlled using heaters and a chiller. The flowmeter and thermocouples are connected to a LabView module to monitor flow rate and temperature during the experiment.

For the measurements using 3T MRI machine, Siemens MAGNETOM TRIO 3T MRI machine at Seoul National University Hospital and an 8 channel phased array torso coil are used. For 7T measurements, PHILIPS 7T Human MRI machine at Korea Basic Science Institute (KBSI) and a 28 channel RF knee coil are used.

For MR measurements, distortion in magnetic field strength due to magnetic susceptibility can result in measurement errors so it must be considered when selecting material for the experiment. For such reason, a 2.0 m long circular transparent PVC pipe is used for

the measurement to minimize this effect. For validation of temperature measurements, the thermocouples are installed at the pipe outlet and the reservoir outlet under the same thermal condition of the MRI scan room before carrying out MR measurements, since a metallic thermocouple cannot be inserted into the test section during the scan. The deviation between the temperatures measured downstream of the flowmeter and at the pipe outlet was less than 0.15℃. Based on this result, the temperature downstream of the flowmeter is considered to be the same as that of the pipe outlet.

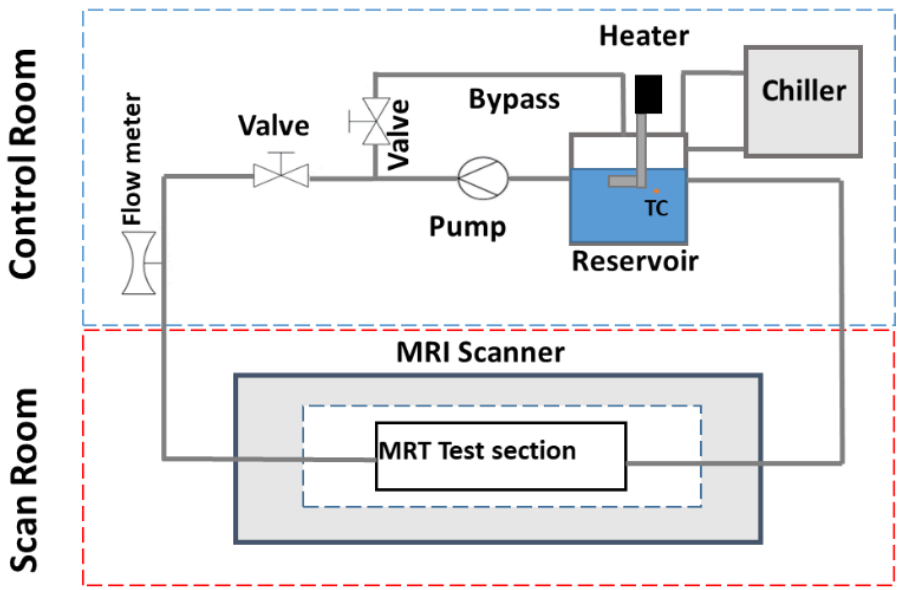

Figure 3.1. Schematic of fully developed pipe flow system

Figure 3.2. Fully developed pipe flow experimental setup (7T MRI)

3.2. Impinging Jet Mixing Flow

Gas turbine combustors are exposed to extreme temperature, and vulnerable to thermal damage. In order to protect major components, a dilution zone, which plays a critical role in terms of thermal mixing, is situated downstream of gas turbine combustors. In this region, jets of coolant are injected radially to control mean temperature and reduce temperature non-uniformity by enhancing thermal mixing through jet impingement. To simulate such flow phenomenon in a gas turbine combustor dilution zone, two separate water reservoirs with different temperatures, which are controlled using heaters and a chiller, are used. Flow conditions are controlled using valves and bypass flow passages attached to each flow loop. Also, a valve is attached at the inlet of a hot reservoir so that the flow is uniformly distributed into each water reservoir for consistency. Similar to the pipe flow case, temperatures and flow conditions are monitored using a LabView module. A schematic of the

flow system is shown in Figure 3.3.

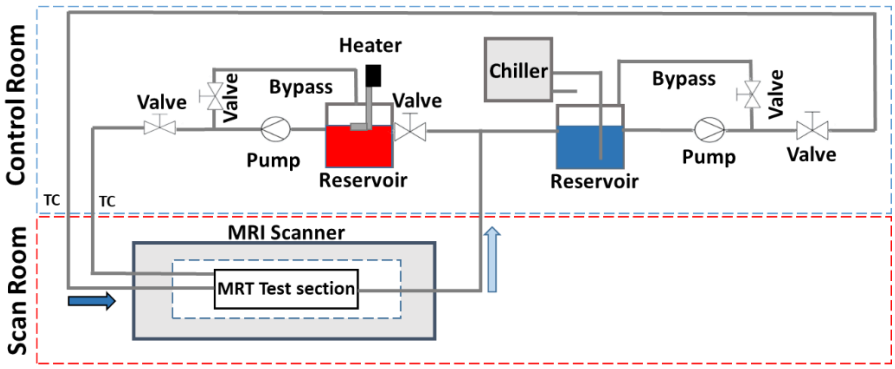

Figure 3.3. Schematic of impinging jet mixing flow system

In the test section, six circular jet holes with diameter of 5.5 mm are placed radially along the pipe wall as shown in Figure 3.4 to generate impinging jets. For fully developed pipe flow, a 2.0 m long acrylic circular pipe with an internal diameter of 50 mm is used for the experiment. Secondary hot flow is inserted into an annular plenum around the pipe and then injected into the main pipe through the jet holes. Flow conditions are controlled using flowmeters, thermocouples, and LabView module. More detailed flow conditions are provided in Chapter 4.

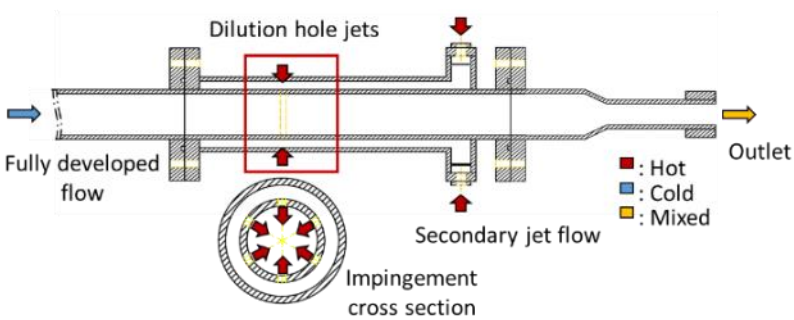

Figure 3.4. Impinging jet mixing flow test section

Chapter 4. Results and Discussion

4.1. Fully Developed Turbulent Pipe Flow

4.1.1. MRV Results

MRV measurement of fully developed turbulent pipe flow is carried out using 40 mM copper sulfate solution with spatial resolution of [x, y, z] = [0.5 mm, 0.5 mm, 1.0 mm] at Reynolds number of 11,700. Z−axis represents streamwise direction and x−axis and y−axis represent cross sectional planar coordinates. 4 scans are conducted for data averaging. In order to check whether the flow is fully developed, the MRV data is compared with DNS data of a fully developed turbulent pipe flow at Reynolds number of 11,700 [15]. MRV result normalized by maximum streamwise velocity and pipe radius is shown in Figure 4.1 along with DNS data.

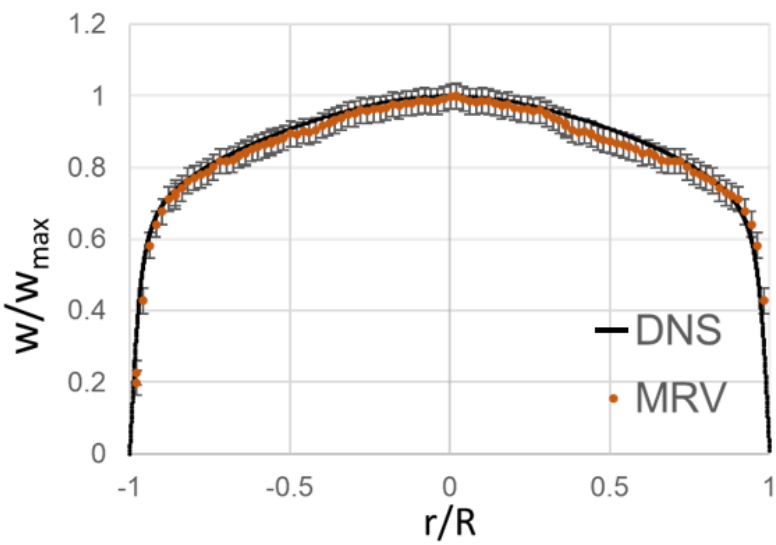

Figure 4.1. Velocity profile of MRV and DNS data for fully developed turbulent pipe flow at Re = 11,700

MRV measurement error is calculated based on Equation 4.1 with 95% confidence interval. The error is calculated based on variance of background noise of the measured phase data.

$$\sigma_{ROI} = \frac{VENC}{\pi}\sqrt{\frac{Var\{\Delta\phi_1(r_{ROI}) - \Delta\phi_2(r_{ROI})\}}{2}} \qquad Equation\ 4.1$$

σ_{ROI} represents the statistical velocity error obtained due to background noise. $\Delta\phi_1$ and $\Delta\phi_2$ each represent signal phase change due to fluid movement. The uncertainty is calculated from the background noise, which is the difference between repeated measurements. The factor 2 in the denominator derives from the subtraction of the phase data.

4.1.2. MRT Results

Measurement parameters for the 3T MRT experiment are provided in Table 4.1. The parameters are referenced from the MRT experiment led by Buchenberg et al. [16]

Table 4.1. 3T MRT scan parameters

ROI	[x, y, z] = [128 mm, 128 mm, 20 mm]
Spatial resolution	[x, y, z] = [0.5 mm, 0.5 mm, 1 mm]
Cases	1−1) Flow on without FC 1−2) Flow off without FC 2−1) Flow on with FC 2−2) Flow off with FC
Temperature conditions	24.3°C (baseline) 34.1°C (target)
Scan #	4 scans for each case
TR, TE, FA	TR : 29 ms, TE : 20 ms, FA : 7°

For the 3T MRT experiment, two different temperature conditions are chosen with total deviation of 9.8°C. The measured signal phase data is corrected using oil reference phantoms in Figure 4.2. By placing oil reference phantoms around the pipe, reference phase data can be obtained to sort out system bias in the data [17].

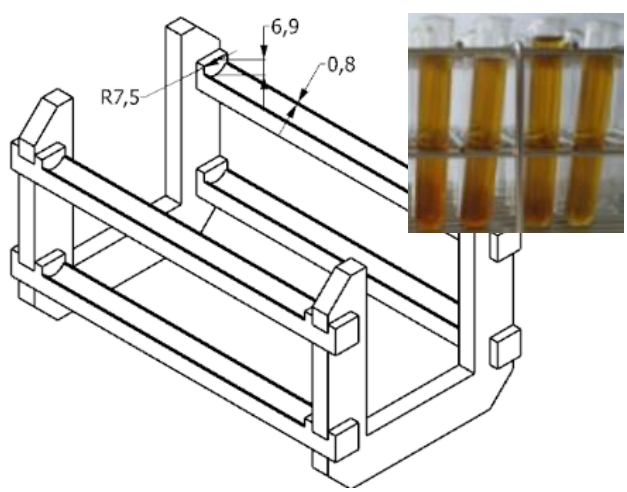

Figure 4.2. Oil reference phantoms and stand

Reference phantoms containing oil are scanned along with the circular pipe. Since oil inside the phantoms are stationary and assumed to have constant temperature, the resultant phase should be uniform within the regions of the phantoms. Due to system bias, however, the phase data obtained from the reference phantoms are not uniform so further data correction is conducted to remove the bias.

For data correction processes, phase data within the oil reference phantom region is first unwrapped to remove any aliasing since oil has phase offset due to chemical shift. Once the data is unwrapped, system bias field is then generated by interpolating / extrapolating the data of the reference phantoms as shown in Figure 4.3 using a MATLAB code [18]. The system bias field is then subtracted from the original phase map for data correction.

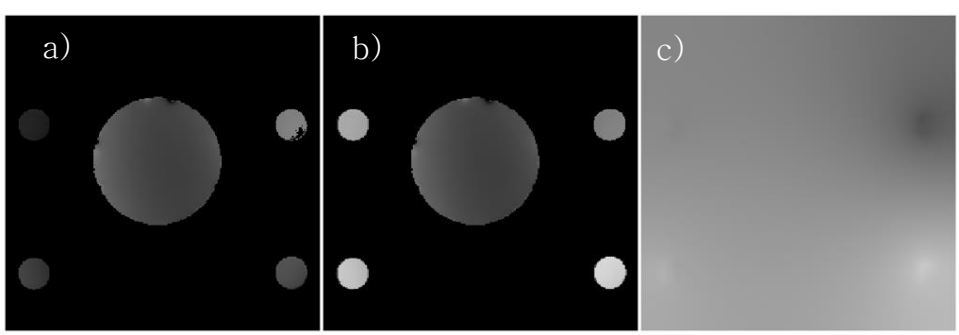

Figure 4.3. (a) Original phase map, (b) Unwrapped phase map, (c) System bias field

Using the resultant phase map, signal phase shift data is converted into temperature data using Equation 2.5 and the results

are shown in Figure 4.4 and Figure 4.5. The resultant temperatures are calculated by averaging temperatures within the regions marked with black squares in Figure 4.4.

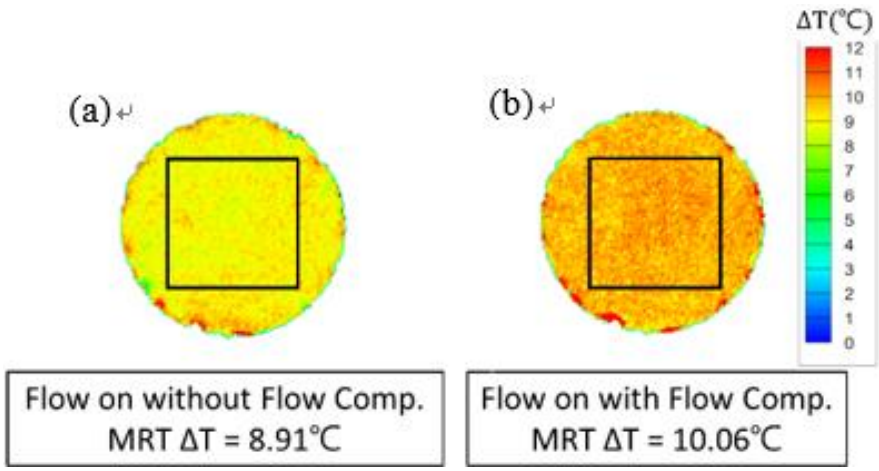

Figure 4.4. Effect of flow compensation
(Center square : 60 x 60 voxel area for data averaging)

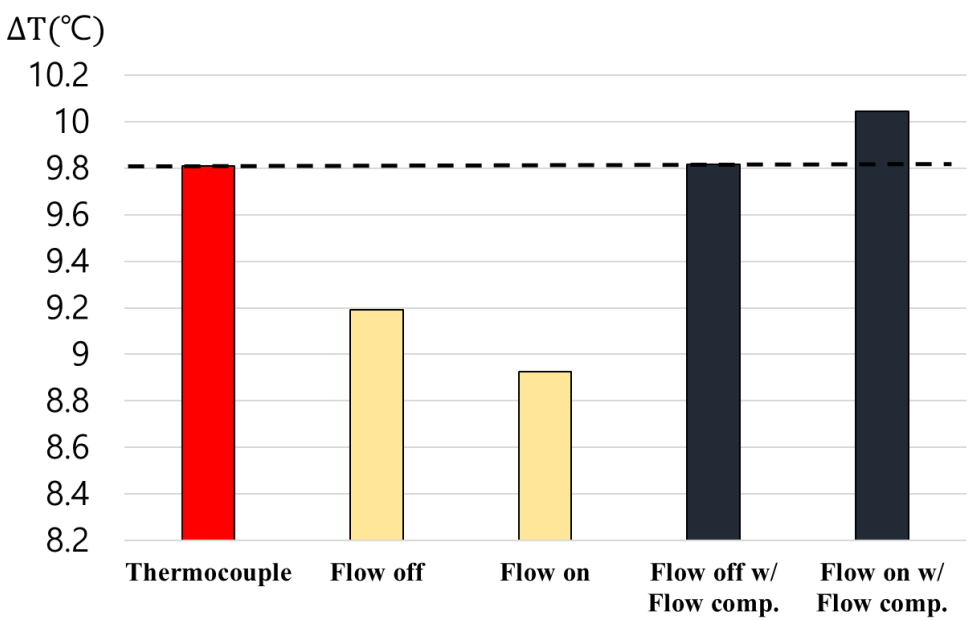

Figure 4.5. Temperature comparison between thermocouple and 3T MRT data

To verify flow compensation technique, sets of data are acquired under “flow on” condition. Figure 4.4 (a) represents MRT result without flow compensation and Figure 4.4 (b) represents the result with flow compensation. The results show that the data with flow compensation shows much better agreement with temperature measured with a thermocouple.

For more detailed analyses, 4 different measurement cases are chosen as listed in Table 4.1. As shown in Figure 4.5, MRT results without flow compensation, which are represented by yellow bars, show larger error, inferring that velocity components are not removed properly. On the other hand, flow compensated measurement data represented by black bars in Figure 4.5 shows much better agreement with thermocouple data. The results show that the effects of velocity on measurement data are successfully eliminated and only the effects of temperature are measured by using flow compensation technique. Based on the results, flow compensation is applied in further MRT experiments.

Similarly, the 7T MRT experiment is conducted with 20 mM copper sulfate solution to maximize signal quality. Experimental parameters are provided in Table 4.2.

Table 4.2. 7T MRT scan parameters

ROI	[x, y, z] = [128 mm, 128 mm, 20 mm]
Spatial resolution	[x, y, z] = [0.5 mm, 0.5 mm, 1 mm]
Temperature conditions	20.3℃ (baseline), 25.3℃, 30.3℃, 35.3℃, 40.3℃
Scan #	4 scans for each temperature case
TR, TE, FA	TR : 25 ms, TE : 13 ms, FA : 7°

For the 7T MRT experiment, additional temperature conditions are selected for further verification of MRT technique. Similar to the 3T MRT experiment, 4 scans are conducted for each temperature case. As previously demonstrated, the experiment is carried out using flow compensation. The results are shown in Figure 4.6 and Table 4.3.

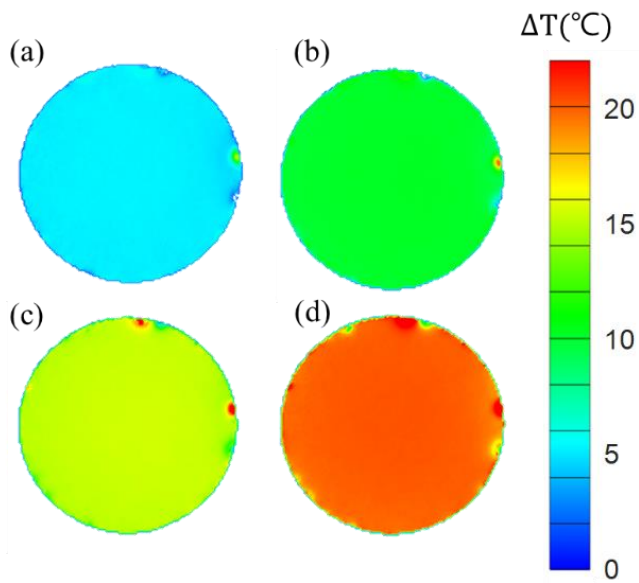

Figure 4.6. 7T MRT temperature maps
(a) ⊿T = 5℃, (b) ⊿T = 10℃,
(c) ⊿T = 15℃, (d) ⊿T = 20℃

Table 4.3. Temperature comparison between thermocouple and 7T MRT data

Case	Thermocouple ⊿T	MRT ⊿T
⊿T = 5℃	5.0 ± 0.1 ℃	5.2 ± 0.1 ℃
⊿T = 10℃	10.0 ± 0.1 ℃	10.3 ± 0.1 ℃
⊿T = 15℃	15.0 ± 0.1 ℃	15.3 ± 0.2 ℃
⊿T = 20℃	20.0 ± 0.2 ℃	20.5 ± 0.2 ℃

The resultant temperatures are calculated from the same region marked in Figure 4.4, and MRT results show good agreement with thermocouple data with relatively small errors as shown in Table 4.3. Measurement uncertainties are calculated from standard deviation of temperature within the center square region.

The PRF thermal constant may vary in value depending on the type of fluid used in the experiment. The previous results provided in the current study are calculated using $\alpha = -0.01$ ppm/℃, which is the PRF thermal constant of pure water found from precise NMR experiments [10−13]. Based on the 7T MRT result from which precision measurements are performed through higher SNR, a new PRF thermal constant for 20 mM copper sulfate solution used in the experiment is derived. An attempt to find a linear relationship between the mean value of the MRT and the thermocouple data is carried out. As a result, a new constant of $\alpha = -0.01106$ ppm/℃ is found and the average error is found to be less than 0.14℃ as shown in Figure 4.7.

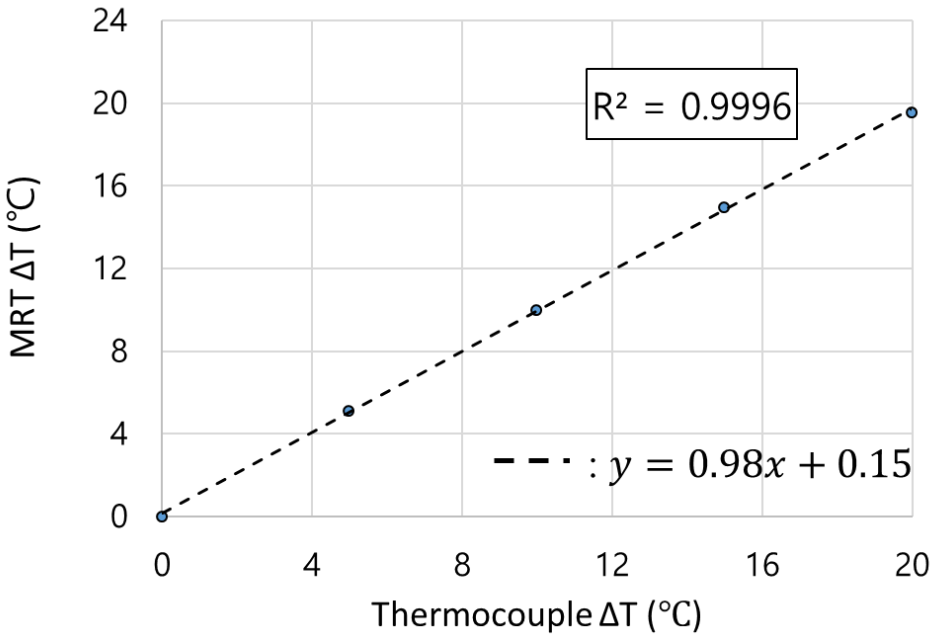

Figure 4.7. Linearity between MRT and thermocouple
(α = − 0.01106 ppm/°C)

4.2. Impinging Jet Mixing Flow

4.2.1. 7T MRV Results

Analysis of jet impingement has been conducted in a number of engineering fields for its wide applicability. Due to its intricate flow structure and physics, however, experimental analysis of jet impingement is challenging. Previous studies on impinging jet mixing flow [19, 20] have shown that the flow pattern can be characterized with a parameter known as momentum flux ratio (J) shown in Equation 4.2.

$$J = \frac{\rho_j V_j^2}{\rho_m V_m^2} \qquad Equation\ 4.2$$

V_j is the velocity of impinging jet and V_m is the velocity of the main cross flow. ρ represents the respective fluid density.

Table 4.4. Experimental conditions (MRV)

Criteria	MRV
ROI	[128 mm, 128 mm, 90 mm (−30 ~ 60 mm)]
Spatial Resolution	[0.5 mm, 0.5 mm, 1 mm]
TR, TE, FA	25 ms, 4 ms, 7 deg.
$J^{1/2}$	25
Mean velocity (cm/s)	Jet : 22
	Main : 0.9
Temperature	24.3 ℃

MRV results clearly show the stagnation point at the center of jet−in−plane (JIP) due to radially injected jets as illustrated in Figure 4.8. In addition, the collision of jets result in strong flow in both directions, where invasive reverse flow occurs in the upstream region interfering with the main flow and jet−like downstream generating higher temperature core region in the downstream region as shown in Figure 4.9. This upstream penetration and downstream jet−like flow result in complex mixing phenomenon.

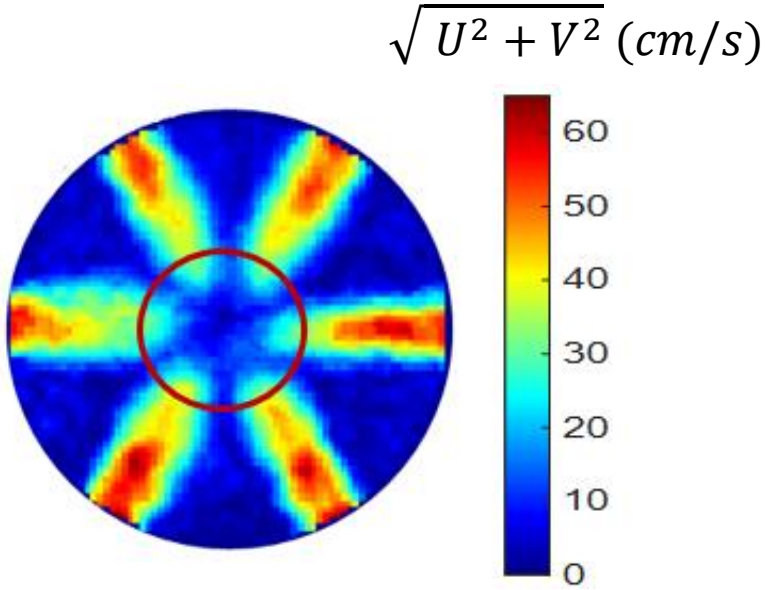

Figure 4.8. Planar view of JIP with stagnation point

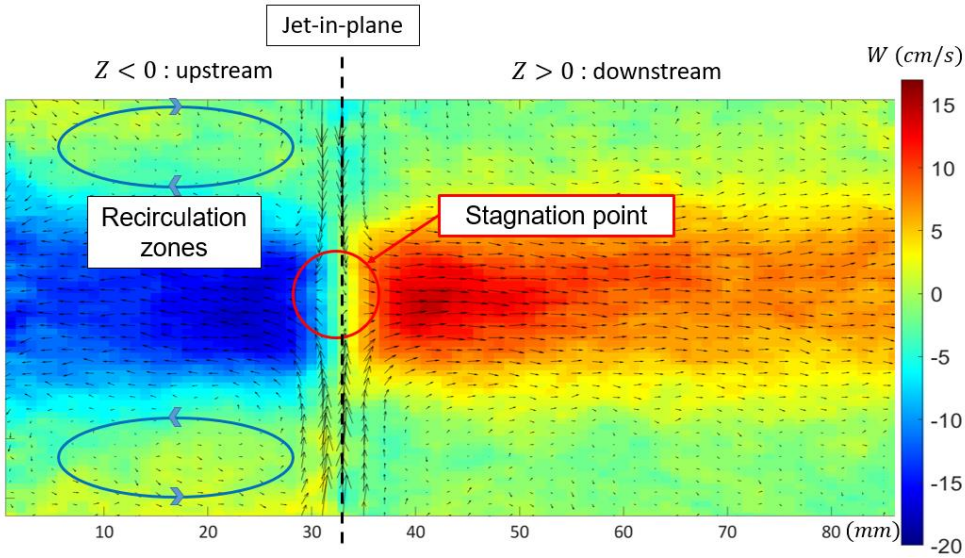

Figure 4.9. Centerplane streamwise velocity field

Based on the MRV data, downstream jet-like flow structure is compared with round free jet [21] using self-similarity analysis. Here, velocity profiles at four different locations downstream are

used for the analysis.

The result shows good agreement between the round free jet and jet-like flow structure as shown in Figure 4.10, which infers that initial flow development in the downstream region of the impinging jet resembles the flow development of a round free jet and the flow mechanism of both flows is analogous. Due to limited ROI of the measurement, wall confinement is not visible from the current result. However, wall confinement effect is expected to affect flow development further downstream and eventually alter the flow into an internal pipe flow.

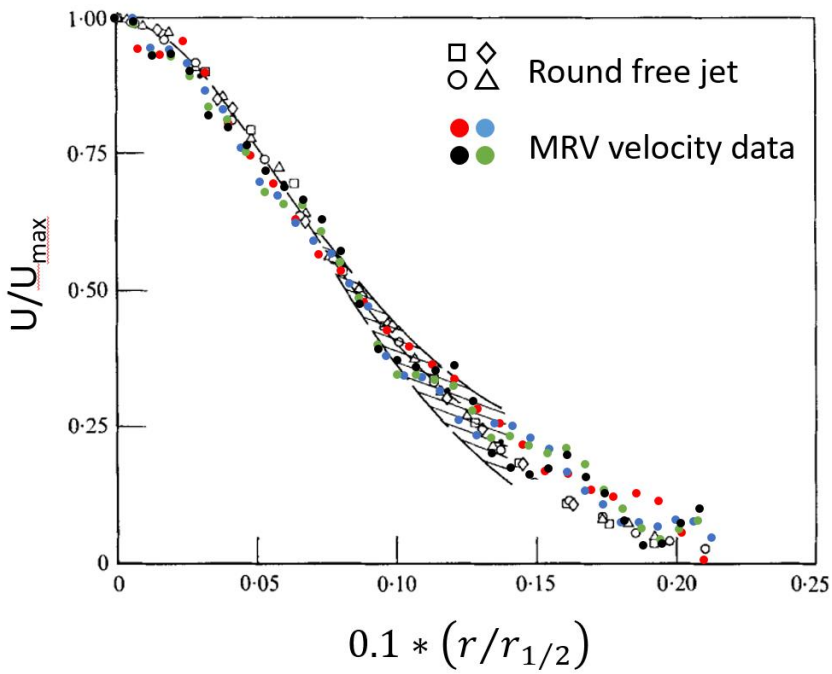

Figure 4.10. Self-similarity analysis of a round free jet (Re # = 10^5) and downstream of impinging jet mixing flow

4.2.2. 7T MRT Results

For the MRT experiment, three different $J^{1/2}$ values are chosen to observe the effects of J on thermal mixing. Experimental conditions are provided in **오류! 참조 원본을 찾을 수 없습니다.**.

Table 4.5. Experimental condition (MRT)

Criteria	MRT		
ROI	[128 mm, 128 mm, 90 mm (−30 ~ 60 mm)]		
Spatial resolution	[1 mm, 1 mm, 1 mm]		
TR, TE, FA	25 ms, 13 ms, 7 deg.		
$J^{1/2}$	15	20	25
Mean velocity (cm/s)	Jet : 22	Jet : 22	Jet : 22
	Main : 1.5	Main : 1.1	Main : 0.9
Temperature	19.8 ℃ (main), 30.4 ℃ (jet) 24.3 ℃ (baseline)		

Note that spatial resolution is bigger for the MRT experiment than that of the MRV experiment to reduce overall scan time and minimize temporal phase drift errors.

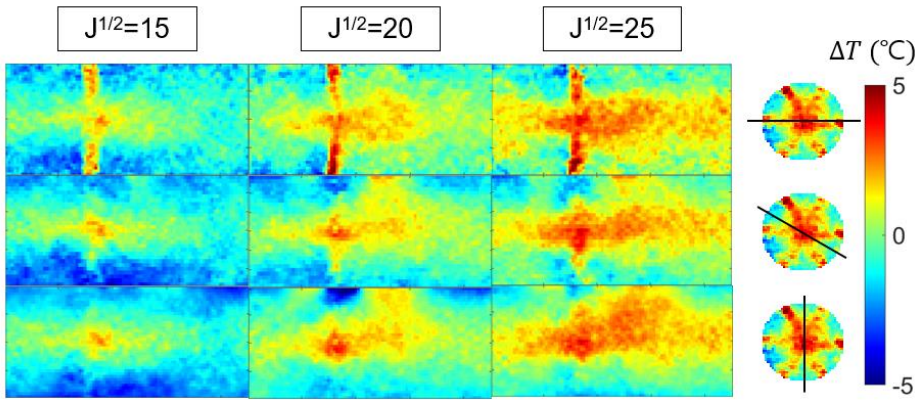

Figure 4.11. Centerplane temperature distribution

In Figure 4.11, a tendency where high temperature region downstream becomes more distinctive and wider due to stronger jet impingement with increasing momentum flux ratio is observed. Temperature non-uniformity is calculated using Equation 4.3 [22] for further data comparison.

$$f_i = \frac{T_i - T_j}{T_m - T_j},\ f_{eq} = \frac{G_j/G_m}{1 + G_j/G_m}\ \ (G = \text{flow rate})$$

$$f' = \sqrt{\frac{1}{A}\sum_i \beta_i \left(f_i - f_{eq}\right)^2} \qquad \textit{Equation}\ 4.3$$

f_i is local mixture fraction, which is the local temperature normalized with jet and main flow temperatures at each voxel within the ROI. f_{eq} is equilibrium mixture fraction for mixed out temperature calculated from flow rate ratios. β_i is local voxel area, and A is total area.

Experimental data from the previous research [22] is compared

with the present MRT data. The previous research focused on the effect of jet-hole geometries on thermal mixing performance. As the current study is based on circular jet-hole geometry, the result of the baseline geometry case is employed for direct comparison. Both experiments are conducted under three momentum flux ratios. The result and the ratios are shown in Figure 4.12. Since the result of the previous research only provides data up to Z/R = 1, the location is marked with a black dotted line on the current experimental data.

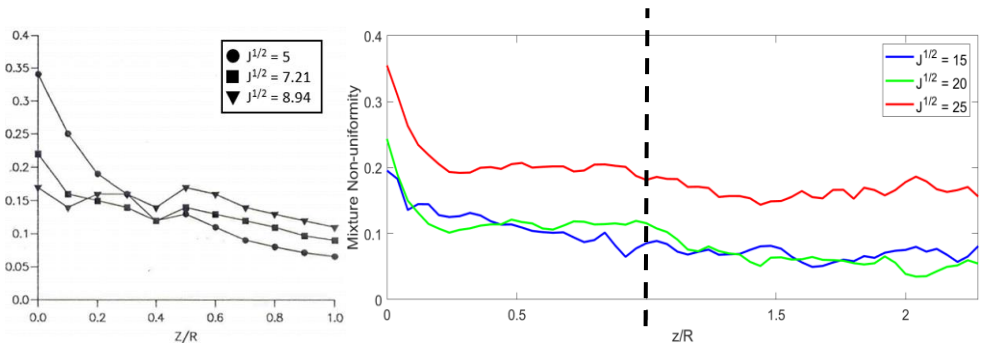

Figure 4.12. Temperature non-uniformity comparison
(left : Hatch et al. [21], right : MRT data

Temperature non-uniformity is an area-weighted standard deviation of temperature, which represents the degree of non-mixedness. So, if the value is nearly zero, then it means that the temperature distribution is almost uniform. As shown in Figure 4.12, tendency of high non-uniformity is visible due to jet injection near the JIP (z/R = 0). Stronger jet penetration in both upstream and downstream regions are observed due to high momentum of flow in the core region due to jet impingement. As the flow progresses

further downstream, shear layer mixing and spreading take place. The temperature in the region is mitigated as the flow is mixed out and the temperature distribution becomes more uniform as shown in Figure 4.11. As a result, change in temperature non-uniformity becomes more gradual as the flow mixed out and thermal mixing is no longer dominant as shown in Figure 4.12.

A tendency where non-uniformity remains relatively high with higher momentum flux ratio is visible in both cases. However, the result of the current study shows that there is no significant difference between J = 20 and J = 15, which infers that increasing the momentum flux ratio does not simply increase the non-uniformity, but rather an optimal condition of mixing exists. Once past the point, temperature non-uniformity is expected to increase due to more dominant downstream "jet-like" flow structure after jet impingement.

As shown earlier, the resultant flow shoots out in both directions generating upstream penetration, a reverse flow in the upstream region with higher temperature due to stagnation of impinging jets, and downstream "jet-like" flow. With higher momentum flux ratio, the downstream flow structure advects further downstream. As the hot center region is maintained further downstream due to higher momentum, mean temperature increases but mixing efficiency decreases as the temperature distribution becomes less uniform increasing the non-uniformity.

4.3. 7T MRT Uncertainty Analysis

4.3.1. Fully Developed Turbulent Pipe Flow

Measurement uncertainty of MR based measurement techniques can be calculated from the statistical approach of the measured signals. Uncertainties of fully developed turbulent pipe flow MRT experiments are calculated using standard deviation of the result within the ROI. Since the flow is fully developed and by assuming adiabatic condition, temperature distribution within the ROI should be uniform. From this perspective, standard deviation of temperature is calculated using the data within the square regions shown in Figure 4.4. In order to minimize the effects of miscellaneous artifacts near the pipe wall, the region is selected at the center region of the pipe. To assure 95% confidence interval, the standard deviation is multiplied by 1.96. The result is shown in Table 4.3.

Also, signal-to-noise ratio (SNR) analysis is essential when evaluating MR data uncertainty. SNR of 3T and 7T MRT data was quantified to identify the characteristics of each experimental data. As shown in Equation 4.4, two region method is used to calculate the SNR from the ratio of the mean signal intensity within the pipe and the standard deviation of the signal intensity of the background noise signals.

$$\mathrm{SNR} = \frac{m(S_{ROI})}{\sigma(S_{background})} \qquad Equation\ 4.4$$

S represents the signal intensity and m and σ represent mean and standard deviation respectively.

In MR measurements, the SNR of the measurement data increases by the square root of the number of ensemble averages through repeated measurements. In this study, since the measurement was conducted 4 times for all flow cases, the SNR of the averaged data is 2 times larger than that of a single measurement. Table 4.6 shows the SNR of the results of 3T and 7T MRT experiments. For direct comparison, only the flow compensated data is shown in the table.

Table 4.6. MRT SNR comparison (pipe flow)

		Single Image SNR	Averaged Image SNR
3T	T = 25.1℃	15.1	27.9
	T = 34.9℃	16.2	29.1
7T	T = 20.3℃	148	314
	T = 25.3℃	142	290
	T = 30.3℃	144	311
	T = 35.3℃	143	283
	T = 40.3℃	145	294

In the case of SNR calculated from a single image, the average of 4 individual datasets is used. The result confirms that the SNR increases about 2 times through the signal ensemble averaging.

The SNR in MR measurement can be changed due to various

reasons including the magnetic field strength, type of RF coil, and the number of transceiver coil channels [23−25] so it is hard to say that the difference in SNR between 3T MRT and 7T MRT results is caused only by the difference in external magnetic field strength. As mentioned earlier in the paper, 8 channel phased array torso coil is used for 3T MRT experiment and 28 channel knee coil is used for 7T experiment. Also, for the 3T MRT experiment, 40 mM solution used in the previous MRV experiment is used for the experiment. On the other hand, the solutions with 10 different concentrations are tested to maximize signal intensity for the 7T MRT experiment. For such reasons, the SNR for the 7T MRT experiment is almost 10 times larger than that of the 3T MRT experiment. As shown in Figure 4.13, it can be seen that the temperature distribution of the 7T MRT result is relatively uniform due to the higher SNR.

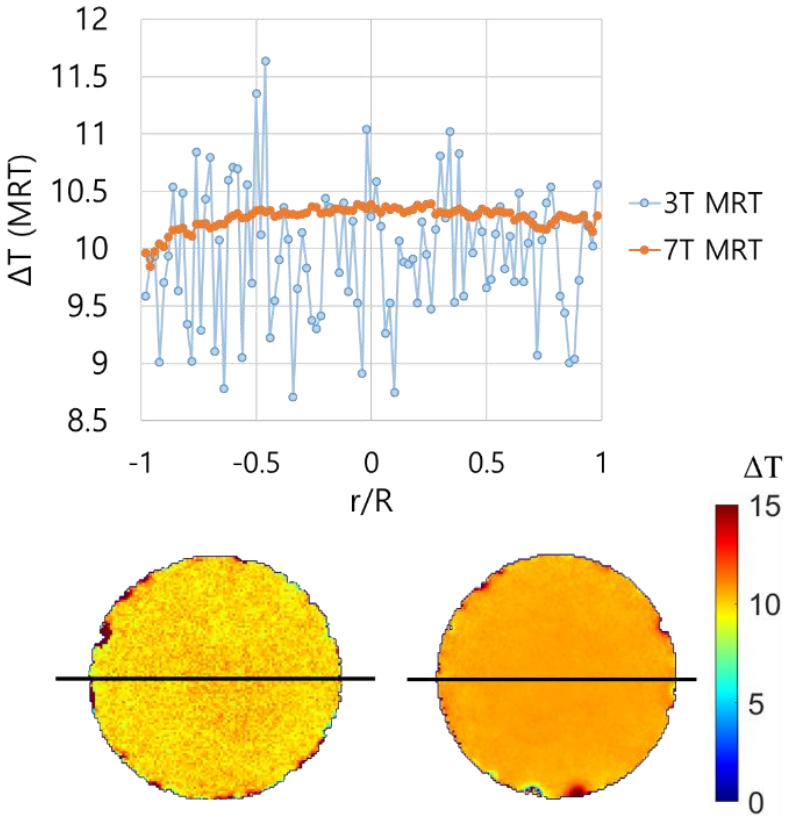

Figure 4.13. Data quality analysis
(a) 3T, (b) 7T (ΔT=10°C)
(ΔT plotted along the centerline)

4.3.2. Impinging Jet Mixing Flow

Similar to the pipe flow experiment, SNR is computed based on the statistical approach. However, since the temperature distribution is no longer uniform due to complex mixing, standard deviation is calculated using SNR and MR parameters as shown in Equation 4.5 [26, 27].

$$\sigma(T) = \frac{\sigma(\phi)}{\gamma \alpha B_0 TE} = \frac{1}{\gamma \alpha B_0 TE} \frac{1}{SNR} \qquad Equation\ 4.5$$

For 95% confidence interval, the standard deviation is multiplied by 1.96. The result is shown in Table 4.7.

Table 4.7. Impinging jet mixing flow SNR and uncertainty

Image SNR	MRT Uncertainty
12.5	± 0.6℃

The SNR is significantly lower compared to that of 7T MRT pipe flow experiment. This is due to much higher background noise caused by complex mixing flow and single measurement without averaging.

Chapter 5. Conclusion

Basic verifications of MRV and MRT are conducted using a fully developed turbulent pipe flow. 3D mean velocity and temperature fields are successfully measured and both qualitative and quantitative analyses are carried out to verify the measurement techniques. Mean velocity field shows good accordance with DNS data and the measured temperature deviation field well corresponds to the temperature measured with thermocouples.

The techniques are further utilized to analyze complex mixing flow by examining radial jet impingement with a cross pipe flow to simulate a combustor dilution zone. The mean velocity field shows a stagnation point at the center of JIP and high temperature core region is also observable due to jet-like flow structure downstream. In addition, development of the jet-like flow structure derived from the jet impingement showed similarity with a round free jet.

Not only has the momentum flux ratio affected mean temperature downstream, but also influenced the mixture non-uniformity. The results show overall increase in temperature as the influence of jet flows become more dominant, and the mixture non-uniformity also increases due to stronger core structure, diminishing mixing efficiency downstream within the ROI.

One of the major purposes of dilution zone in a gas turbine combustor is to enhance flow mixing to remove extreme temperature

gradient or hot-streaks to avoid thermal fatigue damage on turbine blades. The results shown in the present study suggest that momentum flux ratio must be implemented with caution regarding thermal mixing and aerodynamic loss. Higher momentum flux ratio is favorable when quick change in average temperature is required. In terms of temperature uniformity, however, momentum flux ratio must be chosen accordingly through precise aerothermal analysis. Also, jet impingement results in upstream penetration, which causes interference with the main flow is expected to result in aerodynamic loss.

Bibliography

1) Elkins, C.J., Markl, M., Pelc, N., and Eaton, J.K., 2003, "4D Magnetic resonance velocimetry for mean velocity measurements in complex turbulent flows", Exp. In Fluids, Vol. 34, pp. 494−503.
2) Benson, M.J., Elkins, C.J., Yapa, S.D., Ling, J.B., and Eaton, J.K., 2012,"Effects of Varying Reynolds Number, Blowing Ratio, and Internal Geometry on Trailing Edge Cutback Film Cooling", Exp. Fluids, Vol. 52(6), pp. 1415-1430.
3) Wyatt, C., Soher, B., Maccarini, P., Charles, H.C., Stauffer, P., and Macfall, J., 2009, "Hyperthermia MRI temperature measurement: Evaluation of measurement stabilization strategies for extremity and breast tumors", Int. J. Hyperthermia, Vol. 25(6), pp. 422−433
4) Fite, B. Z., Liu, Y., Kruse, D. E., Caskey, C. F., and Walton, J. H., 2012, "Magnetic Resonance Thermometry at 7T for Real−Time Monitoring and Correction of Ultrasound Induced Mild Hyperthermia", PLoS ONE 7(4)
5) Wassermann, F., Buchenberg, W., Simpson, R., Jung, B. and Grundmann, S., 2014, "Applying Magnetic Resonance Thermometry to Engineering Flows", 17th Int. Symposium on Applications of Laser Techniques to Fluid Mechanics.
6) Spirnak, J., Samland, M., Tremont, B., McQuirter, A. Williams, E., Benson, M. J., Poppel, B., VerHulst, C., Elkins, C. J., Burton, L., Eaton, J. K., and Owkes, M., 2016, "Validation of Magnetic Resonance Thermometry through Experimental and Computational Approaches", AIAA Propulsion and Energy, 10.2514/6.2016−4741.
7) Benson, M.J., Poppel, B., Elkins, C.J., Owkes, M., 2019, "Three−Dimensional Velocity and Temperature Field Measurements of Internal and External Turbine Blade Features Using Magnetic Resonance Thermometry", J. of Turbomachinery, Vol. 141(7)
8) Curry, T., Dowdey, J., and Murry, R., *Christensen' s Physics of Diagnostic Radiology 4th Ed.*, Lippincott Williams & Wilkins., 1990
9) Rieke,V. and Pauly, K. B., 2008, "MR Thermometry", J. Magn. Reson. Imaging, Vol. 27(2), pp. 376−390.
10) Schneider, W.G., Bernstein, H.J., and Pople, J.A., 1958, "Proton Magnetic Resonance Chemical Shift of Free (gaseous) and Associated (liquid) Hydride Molecules", J. Chem. Phys., Vol. 28, pp. 601−607.
11) Norbert Muller, 1965, "Concerning Structural Models for Water and Chemical−shift Data", J. Chem. Phys., Vol. 43, pp. 2555−2556.
12) Hindman, J.C., 1966, "Proton Resonance Shift of Water in the Gas and Liquid States", J. Chem. Phys. Vol. 44, pp. 4582−4592.
13) Muller, N. and Reiter, R., 1965, "Temperature Dependence of Chemical Shifts of Protons in Hydrogen Bonds", J. Chem. Phys., Vol. 42, pp. 3265−3269.
14) Yuan, C., Gullberg, G., and Parker, D., 1989, "Flow−Induced Phase Effects and Compensation Technique for Slice−Selective Pulses",

Magnetic Resonance Medicine, Vol. 9, pp. 161−176.
15) Khoury, G., Schlatter, P., Noorani, A., Fischer, P., Brethouwer, G., and Johansson, A., 2013, “Direct Numerical Simulation of Turbulent Pipe Flow at Moderately High Reynolds Numbers”, Flow, Turbulence and Combustion, Vol. 91, pp. 475−495.
16) Buchenberg, W., Wassermann, F., Grundmann, S., Jung, B, and Simpson, R., 2016, “Acquisition of 3D Temperature Distributions in Fluid Flow Using Proton Resonance Frequency Thermometry”, Magnetic Resonance in Medicine, Vol. 76, pp. 145−155.
17) Oh, S., Ryu, Y., Carluccio, G., Sica, C., and Collins, C., 2014, “Measurement of SAR−Induced Temperature Increase in a Phantom and In Vivo with Comparison to Numerical Simulation”, Magnetic Resonance in Medicine, Vol. 71, pp. 1923−1931.
18) John D'Errico (2019). Inpaint nans, (https://www.mathworks.com/matlabcentral/fileexchange/4551−inpaint_nans), MATLAB Central File Exchange. Retrieved July 2nd, 2019.
19) Kartaev, E.V., Emelkin, V.A., Ktalkherman, M.G., Aulchenko, S.M., and Vashenko, S.P., 2018, “Upstream penetration behavior of the developed counter flow resulting from multiple jet impingement in the crossflow of cylindrical duct”, Intl. J. of Heat and Mass Transfer, Vol. 116, pp. 1163−1178
20) Muirhead, K. and Stephen, L., 2019, “Computational Study of Combustor Dilution Flow Interaction with Turbine Vanes”, J. of Propulsion and power, Vol. 35, pp. 54−71
21) Wygnansky, I. and Fielder, H., 1969, “Some measurements in the self−preserving jet”, J. Fluid Mech., Vol. 38, pp. 677−612
22) Hatch, M.S., Sowa, W.A., Samuelsen, G.S., Holdeman, J., 1992, “Jet Mixing Into a Heated Cross Flow in a Cylindrical Duct: Influence of Geometry and Flow Variations”, AIAA 30th Aerospace Sciences Meeting and Exhibit
23) Childs, A.S., Malik, S.J., O’ Regan, D.P., and Hajnal, J.V., 2013, “Impact of number of channels of RG shimming at 3T”, Magn. Reson. Mater. Phy., Vol. 26, pp. 401−410
24) Katscher, U. and Bornert, P., 2006, “Parallel RF transmission in MRI”, NRM Biomed., Vol. 19, pp. 393−400
25) Gruber, B., Froeling, M., Leiner, T., and Klomp, D., 2018, “RF coils: A practical guide for nonphysicists”, J. Magn. Reson. Imaging, Vol. 48(3), pp. 590−604
26) Conturo, T.E. and Smith, G.D., 1990, “Signal−to−noise in phase angle reconstruction: Dynamic range extension using phase reference offsets”, Magnetic Resonance in Medicine, Vol. 15(3), pp. 420−437
27) Rieke, V., Vigen, K.K., Sommer, G., Daniel, B.L., Pauly, J.M., Butts, K., 2004, “Referenceless PRF Shift Thermometry”, Magnetic Resonance in Medicine, Vol. 51, pp. 1223−1231

자기공명영상법의 적용을 통한 충돌 제트 혼합 유동의 열/유동 분석

서울대학교 대학원
기계항공공학부
류 형 우

요약

복잡한 유동 시스템의 경우 그 성능 평가를 위해 열/유동 해석이 필수적이다. 그러나 복잡한 기하학적 구조와 극한의 조건으로 인해 기존의 계측 방법을 통한 열/유동 계측은 매우 어렵다. 이러한 한계점은 비침습적인 자기공명 기반의 측정 기법으로 극복이 가능하다. 본 연구에서는 자기공명속도계 (MRV) / 온도계 (MRT)를 활용하여 제트가 방사형으로 분사되어 주 유동과 혼합되는 가스터빈 엔진 연소부의 dilution zone을 모사하는 복잡한 열유동의 3차원 평균 유동장 및 온도장 측정을 수행한다. 계측 기법의 기본 검증을 위해 완전발달 난류 원관유동의 열/유동장 계측을 MRV/T를 통해 수행한다. 완전발달 영역에서 직접 수치해석 데이터와 유사한 유동 분포도가 계측되며 열전대 계측 값과 비교를 통해 MRT 기법의 검증을 수행한다.

Dilution zone 분석에서는 제트 충돌로 인해 상류로의 침투와 하류에서의 제트와 유사한 유동 구조가 관찰되며, 하류의 제트와 유사한 유동 구조는 속도 분포상의 정규화를 통한 원형 자유 제트와의 비교를 통해 유동 메커니즘 분석을 수행한다. 또한 3가지 운동량 흐름 비율로 인한 결과 비교를 통해 열 혼합과 운동량 흐름 비율의 상관관계에 대한 연구를 수행한다.

주요어: 자기공명온도계, 자기공명속도계, 열/유동 분석, 가스터빈 연소기, 위상차, 양자공명주파수 변화
학번: 2018-28838